

High-resolution radial $K\alpha$ spectra obtained from a multi-keV electron distribution in solid-density titanium foils generated by relativistic laser–matter interaction

U. Zastrau^{a,*}, A. Sengebusch^b, P. Audebert^c, E. Brambrink^c, R.R. Fäustlin^d, T. Kämpfer^a, E. Kroupp^e, R. Loetzsch^a, Y. Maron^e, H. Reinholz^b, G. Röpke^b, E. Stambulchik^e, I. Uschmann^a, E. Förster^a

^a Institut für Optik und Quantenelektronik, Friedrich-Schiller-Universität, Max-Wien-Platz 1, 07743 Jena, Germany

^b Institut für Physik, Universität Rostock, Wismarsche Str. 43–45, 18051 Rostock, Germany

^c Laboratoire pour l'Utilisation des Lasers Intenses (LULI), UMR 7605 CNRS-CEA-Ecole Polytechnique, Palaiseau, France

^d Deutsches Elektronen-Synchrotron DESY, Notkestrasse 85, D-22607 Hamburg, Germany

^e Faculty of Physics, Weizmann Institute of Science, Rehovot 76100, Israel

ARTICLE INFO

Article history:

Received 20 September 2010

Received in revised form

25 January 2011

Accepted 27 January 2011

Available online

Keywords:

X-ray

Spectroscopy

Laser–matter-interaction

Dense plasmas

Line-shape modeling

Backlighter

Hydrodynamics

Warm dense matter

ABSTRACT

We studied temperature and $K\alpha$ yield radial profiles of thin titanium foils as a result of femtosecond high-power laser pulse irradiation at several 10^{19} W/cm² by high-resolution x-ray spectroscopy. Laser-accelerated electrons heat the cold solid to bulk temperatures of up to ~ 50 eV. The plasma strongly affects the shape of the emitted $K\alpha$ doublet, which is surveyed by x-ray spectroscopy with both high spectral ($E/\Delta E \geq 15,000$) and 1D spatial ($\Delta x \leq 13.5$ μm) resolutions. Temperature-dependent spectra modeled by line-shape calculations are compared with Abel-inverted experimental spectra and provide a radial temperature distribution. The radially resolved $K\alpha$ yield shows a depletion of the $K\alpha_1$ -line at the position of the laser focus. The density gradients induced by prepulses are modeled by hydrodynamic simulations, and density-dependent line-shape models are applied. The x-ray yield as function of foil thickness is explained by partial refluxing of a multi-keV electron distribution inside the foil, supported by Monte-Carlo simulations. Finally, we derive parameters to optimize the peak brilliance of such a laser-driven thin foil x-ray source.

© 2011 Elsevier Ltd. All rights reserved.

1. Introduction

The generation of strongly coupled plasmas gains increasing interest for studying matter in states between cold condensed materials and hot dense plasmas. This so-called warm dense matter (WDM) [1] occurs as a transient state in novel experiments generating high energy plasma in materials and will be of particular importance for the success of inertial confinement fusion [2–4]. This investigation enables the perpetual improvement of key applications including laser-driven sources of x-rays [5], e.g., to serve as backlighters [6,7] or particle accelerators [8–10], providing alternative radiation sources for both scientific and medical applications.

A proper description of strongly coupled plasmas created by relativistic laser–matter interaction poses several challenges. The highly non-linear electron creation and acceleration process leads to the presence of an electron distribution with energies ranging

from keV up to several MeV [11]. Solid targets heated by collisions with these electrons are far from being homogeneous, resulting rather in an essentially non-equilibrium state with steep spatial gradients [12]. Thus, it is of primary importance to achieve precise knowledge of the physical properties, in particular the plasma temperature, with high spatial resolution at solid-density [13].

When an ultrashort ($\tau \leq 500$ fs) laser pulse with intensities of several 10^{19} W/cm² interacts with a solid metal foil, free electrons are created in a depth equivalent to the skin depth (< 100 nm) with a Maxwellian-like temperature distribution [14]. Subsequently, they are accelerated and pushed through the cold solid bulk material, mainly by the ponderomotive forces [15]. Per 1 J incident laser energy, the average current $I = eN/\tau$ carried by N electrons over the laser pulse duration τ amounts to several tens of MA [16]. During the interaction time, the ions cannot follow the electrons because of inertia and very strong electric fields arise due to this charge-separation. Hence, the free bulk electrons form fast rising return currents. Although the fast MeV electrons leave at the foil backside [17], the slower electrons deposit their energy inside the foil. According to computational models [18], magnetic fields of several 100 T may be induced [19].

* Corresponding author.

E-mail address: ulf.zastrau@uni-jena.de (U. Zastrau).

Experimental investigations of WDM have been performed, e.g., in shock wave experiments [20], by using intense particle beams [21–23], optical lasers [12,13,24–26], and, most recently, by using XUV free electron lasers [27,28]. Beyond, measurements of the characteristic inner-shell $K\alpha$ emission have proven to provide powerful and reliable diagnostics for solid-density plasmas. Plasma parameters strongly affect the structure of the emitted lines [29]. In particular, the emergence of blue satellites due to creation of M-shell holes is an indicator for the bulk electron temperature [30,31]. The x-ray emission occurs in an ultrashort burst, allowing determination of the plasma properties within the first picoseconds after laser–matter interaction [5]. In laser–plasma experiments, K-shell transitions occur because of vacancies created by electron impact. The solid-density plasma is penetrable for the emitted x-rays, which, therefore, yield unique information about the target interior. This is a big advantage compared to measurements of XUV or visible radiation which cannot penetrate high density plasma.

In this study, we extend our former work [30] to observations of the x-ray yield with spatial resolution finer than the laser focal spot. Further, the influence of prepulses from the laser are modeled by hydrodynamics simulations, and density-dependent line-shape calculations are applied accordingly. Next, insight into the electron population, responsible for the target heating and $K\alpha$ emission, is gained by comparing the conversion efficiency of the laser to the absolute x-ray photons emitted from different foil thicknesses. Monte-Carlo simulations lead to a model of partially refluxing electrons. With respect to applications of laser-driven x-ray sources, we finally derive parameters to optimize the plasma source emission.

2. Experimental setup and Abel deconvolution

The experiments [30] were performed at the *LULI 100TW* laser facility [32] in Palaiseau, France. At a central fundamental wavelength of $\lambda = 1057$ nm the on-target energy was about 14 J, with a pulse duration of 330 fs. The laser is focused by an off-axis parabola to a focal spot of 8 μm in diameter, yielding intensities $\sim 5 \times 10^{19}$ W/cm². Within the first nanosecond before the main pulse, amplified spontaneous emission (ASE) and prepulses have a contrast ratio of 10^{-8} with respect to the peak intensity. When the laser pulse is frequency doubled ($\lambda = 529$ nm), the intensity is $\sim 2 \times 10^{19}$ W/cm² and the contrast is improved to 10^{-10} . Impinging at 11° to the surface normal (see Fig. 1), the laser is linearly polarized, with the electric field being parallel to x at the fundamental wavelength (ω), and parallel to y when frequency doubled (2ω).

Free standing titanium foils of 2–25 μm thickness as well as bulk material were used as targets. A 5 μm foil was covered by 250 nm of copper to study the influence of the prepulse.

Time-integrated single-pulse spectra of the $K\alpha$ -doublet emission (~ 4.5 keV) are detected using a toroidally bent crystal x-ray spectrometer [33]. It employed a GaAs crystal, toroidally bent to radii of 450 mm in the meridional direction (i.e. the dispersion plane) and 305.9 mm in the sagittal direction. The crystal was placed 245 mm from the plasma source and centered at $E_{\text{photon}} = 4508$ eV (Bragg angle $\Theta = 76.66^\circ$). An x-ray film was placed on the Rowland circle 435 mm from the crystal, as illustrated in Fig. 1. In this configuration, the spectral resolution was determined as $E/\Delta E \geq 15,000$, mainly limited by the measured rocking curve and independent of the plasma size due to the use of the Johann scheme [34]. The spatial resolution in the sagittal direction is about 4 μm [35]. The efficiency of this spectrometer is $N_{\text{det}}/N_0 = 2 \times 10^{-5}$ [33]. All spectra were recorded using absolutely calibrated x-ray film. Applying the known crystal efficiency, we are able to infer absolute photon numbers. The bent crystal spectrometer yields 1D resolved spectra of the plasma emission, as shown in Fig. 2. To obtain an optimal signal-to-noise ratio (SNR) for the spectral analysis, the films were scanned with steps of 13.5 μm along the spatially resolved axis with respect to the plasma dimensions. For the x-ray yield analysis, the data were binned spectrally, allowing for data extraction at very fine steps of 2.8 μm with respect to the plasma dimensions.

For the results in Fig. 2, a 5×10^{19} W/cm² intense laser pulse at ω hits a 10 μm thin Ti foil. The regions far from the laser focus ($y \geq 100$ μm) still emit $K\alpha$ photons, and their shape shows the typical doublet structure of undisturbed titanium spectra. Closer to the laser focus, we observe the same profile and emissivity for all $y \leq 27$ μm . These profiles show a significant blue wing and a rather smooth shape without additional lines. In the intermediate regions, a dramatic change of the profiles is observed with every further step of 13.5 μm . Note that we observe no shifted positions of the $K\alpha_1$ and $K\alpha_2$ components.

The measured spectrum as a function of the coordinates x' and y (as shown in Fig. 1) is the local emissivity integrated along both the x - and z -axes, as indicated by the blue slice in Fig. 1. As the authors have already shown [30], for the thin foils, the foil thickness d is comparable or smaller than the effective absorption length, and the attenuation is rather minor. Besides, spectra obtained from bulk

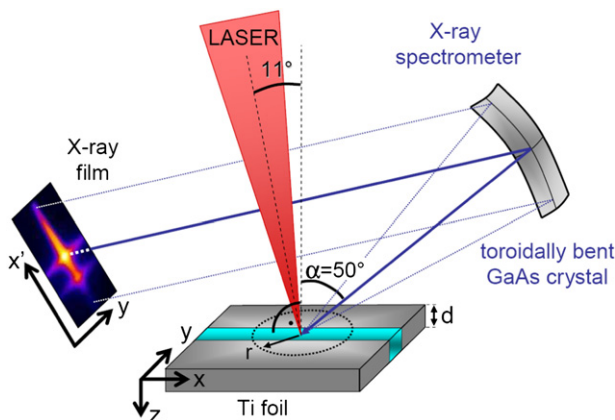


Fig. 1. Schematic of the experimental setup. The energy dispersion axis x' on the x-ray film is perpendicular to the spatial resolution in y -direction [30].

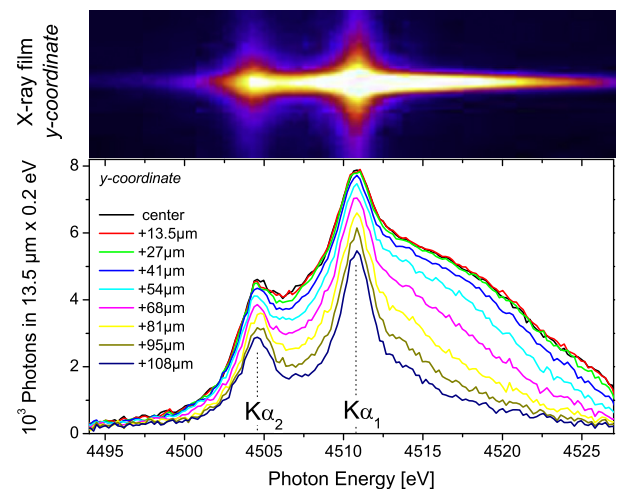


Fig. 2. Single-pulse x-ray spectra of the laser-irradiated 10 μm thick Ti foil at laser intensity $I = 5 \times 10^{19}$ W/cm² and $\lambda = 1057$ nm, shown from different lateral target positions y .

targets represent mostly the radiation from the frontside 20 μm -thick layer.

In order to obtain radially resolved spectra and x-ray yields, Abel inversion is applied. We assume axial symmetry, with the axis perpendicular to the target surface, which is the dominant direction of the electron acceleration process [36]. The spectrum thusly inferred, however, is averaged over d .

The data sets were iteratively Abel-inverted, based on geometry calculations of concentric emission areas A_j^i with a radial index i and a segment index j , as shown in Fig. 3. At a sufficiently large radius, we observe no plasma emission within the spectral range of the x-ray spectrometer. Here, the initial spectrum $S(0)$ is defined, normalized to an emitting unit area, and called $R(0)$.

Next, the spectrum from a lateral strip closer to the center $S(1)$ is treated as a sum of the radial contributions at this position, called $R(1)$, and $R(0)$. The weighting ratio is calculated by the contributing geometrical areas A_j^i . The recapitulatory iteration formula is given by:

$$R(i) = \frac{S(i)}{A_0^i} - \sum_{j=1}^{i-1} \frac{A_j^i}{A_0^i} R(j) \quad (1)$$

Cautious Fourier filtering was applied to the spectroscopic data where the noise level significantly exceeded the $K\alpha$ -signal to avoid accumulation of noise, which can make a reasonable reconstruction impossible.

Fig. 4 shows five selected radially resolved Ti- $K\alpha$ spectra obtained by the Abel transformation of the data presented in Fig. 2. At radii $\geq 100 \mu\text{m}$ we observe a narrow doublet structure (at about 4504 eV and 4511 eV, respectively), similar to those obtained from an x-ray tube. Close to the emission center, a blue wing emerges on both lines. For radii $\leq 30 \mu\text{m}$, the fine structure is completely smeared out, resulting in a broad line profile with a maximum at $\approx 4515 \text{ eV}$, an FWHM of about 20 eV, and an integrated emission an order of magnitude stronger than that at $r = 150 \mu\text{m}$.

3. Radial profiles

In order to analyze the radially resolved spectra with respect to the plasma properties, we calculate titanium $K\alpha$ spectra over a wide range of plasma parameters, i.e. bulk temperatures of $T_e = 4\text{--}100 \text{ eV}$ and free electron densities of $n_e = 10^{22}\text{--}10^{24} \text{ cm}^{-3}$. We apply a perturbative approach: In a first step, the isolated ionic emitters are described via self-consistent Roothaan–Hartree–Fock-equations. In a second step, an additional potential due to the plasma environment is determined. We solve the Poisson equation within a Wigner–Seitz sphere around the considered ion, taking into account contributions of the nucleus as well as surrounding bound

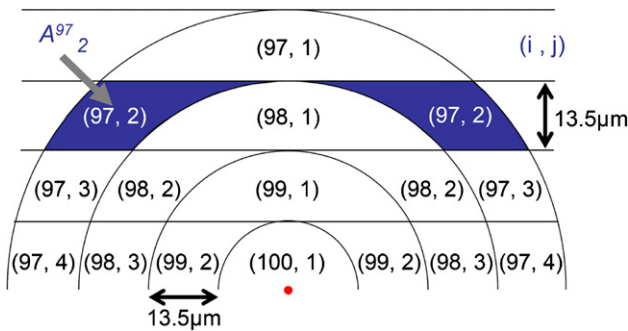


Fig. 3. Illustration of the discrete Abel inversion applied to the measured spectra. The plasma emission is assumed to be cylindrically symmetric and divided into segments with radius index i and segment index j . The emission from a lateral strip is then converted into the emission from a certain radius.

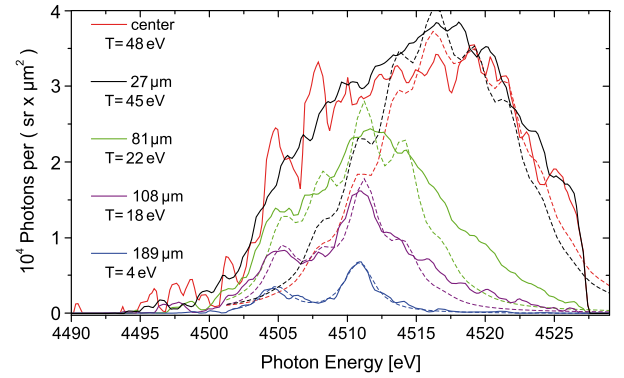


Fig. 4. Comparison of selected Abel-inverted experimental spectra (solid lines) from irradiation of a 10 μm Ti foil, and modeled spectra at the best-fit temperature for each radius (dashed lines).

and free electrons [37]. This ion sphere model is solved fully self-consistently with respect to the free electron density. By means of first order perturbation theory, we calculate shifted emission and ionization energies necessary to explain modified spectral line positions and emitter populations, respectively [38].

In order to build up synthetic spectral line profiles, we have to determine the abundance of different ion species. Assuming local thermal equilibrium, we calculate the plasma composition by a set of Saha equations coupled via the free electron density n_e and the target density. Continuum lowering and the Mott effect are taken into account using the ionic partition functions in Planck–Larkin renormalization [39]. Moreover, the electronic partition function contains quantum statistical corrections to electron–electron and electron–ion interactions, respectively, accounting also for continuum lowering [40].

The calculations involve 12 ionization stages starting from Ti^{4+} , which is the ground state of the ions in the cold titanium foil. For each ionization stage, the ionic partition function contains the ground state as well as three excited states, unless they have merged into the continuum. To achieve physically justified temperature estimates, excited emitter contributions are crucial [38,41]. For example, at $T_e = 20 \text{ eV}$ about 20% of the Ti ions occupy excited states, emitting blue-shifted spectral lines.

In order to obtain spectral line profiles, every shifted emission energy is assigned a Lorentzian profile with a height due to the relative abundance of the emitter state. The Lorentzian width is treated as semi-empirical parameter, taking the cold $K\alpha_2$ -width of 2.1 eV [42]. Finally, the spectra are convoluted with a 0.3 eV wide Gaussian profile to account for the rather small measured instrumental broadening [35]. Radially resolved temperatures are determined by using these theoretical spectra to fit the deconvoluted data.

The best-fit temperature value at each radius was inferred from the Pearson product–moment correlation coefficient closest to one, which was calculated within a spectral range of $\pm 5 \text{ eV}$ around the maximum intensity peak. As seen in Fig. 4, a good agreement was achieved for the central peak at all radii. For higher temperatures, significant contributions of higher ionization stages and excited state satellites affect the line-shape, resulting in the blue shift and broadening of the $K\alpha$ spectrum. Due to large plasma gradients at smaller radii, assuming only one temperature leads to a mis-fit for the red spectral wing. A possible reason is the presence of colder plasma in deeper layers.

Applying the fitting procedure for every data set, T_e is inferred with a 13.5 μm resolution. At radii $\geq 150 \mu\text{m}$ we observe the line-shape of cold titanium. Since the correlation coefficient is sensitive to the slope but not to the intensity of the measured spectra, large

noise in the outer target regions can lead to unphysically high temperature estimates at large radii. Moreover, theoretical line-shapes do not change significantly below $T_e \approx 8$ eV. Thus, we only plot results for the heated target area and cut off the radial profiles, when temperatures drop below 8 eV or start to rise again. The radial temperature profiles for both lower laser contrast (ω) and high laser contrast (2ω) are presented in Fig. 5. The maximum temperature is consistently above 35 eV. At ω , this temperature extends over 10 μm within the bulk, which is about the diameter of the laser focal spot. The heated target radius is increasing for thinner foils up to 80 μm for the 5 μm and 10 μm foils, which is an order of magnitude larger than the laser focus.

For the 2ω exposures, we find the same systematic dependence: both the maximum temperature and the heated area radius rise when the foil thickness decreases. However, the moderately heated (≥ 10 eV) target area is less dependent on foil thickness than for the ω exposures and comparable in size to the bulk target.

The enormous advantage of radially resolved spectra is illustrated by Fig. 6. The spectrum obtained by a non-imaging spectrometer is shown in inset (a), and shows a line-shape of Ti plasma at approximately 8–12 eV temperature when compared to the line-shape calculations discussed above. Inset (b) repeats selected spectra from Fig. 2, which are laterally resolved due to the one-dimensional imaging capability of toroidally bent crystals. Finally, inset (c) shows the radially resolved spectra obtained by Abel inversion of the data from (b). Evidently the line-shape changes much more fundamentally than one would expect from the lateral measurements.

The total radially resolved $K\alpha$ x-ray yield can be determined by integrating over photon energy in the laterally resolved spectra and applying Abel inversion. We investigated the $K\alpha$ yield from the full spectral range of the spectrometer, 4490–4530 eV, see Fig. 7. For comparison, a narrow window of $\Delta\lambda/\lambda = 10^{-3}$, placed around the $K\alpha_1$ -peak at $E = 4510.9$ eV, is analyzed. The overall $K\alpha$ emission shows an increase towards the irradiation center for all investigated foil thicknesses. However, the emission from the $K\alpha_1$ -peak does not exceed a certain threshold of 2.6×10^8 photons/sr/ μm^2 . In case of the exposures at ω , we actually observe a decrease of this emission at radii ≤ 20 μm , i.e. close to the laser focus, because ionization has reduced the number of cold $K\alpha$ emitters significantly.

4. Hydrodynamic motion

The 2ω data from Figs. 5 and 7 show that both temperature and x-ray yield are confined to an area of <60 μm radius, rather

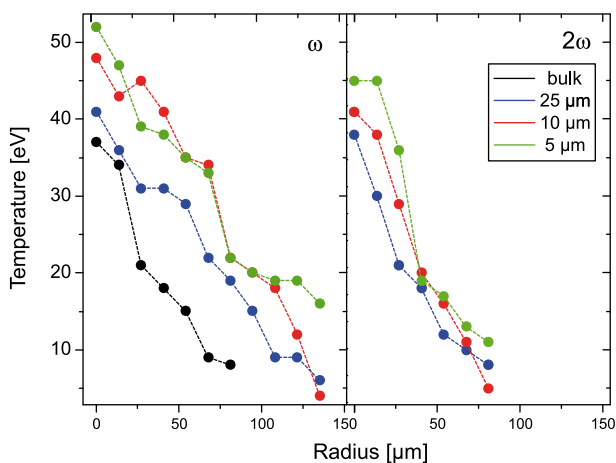


Fig. 5. Radial temperature distributions for various foils thickness, irradiated with both ω and 2ω laser pulses.

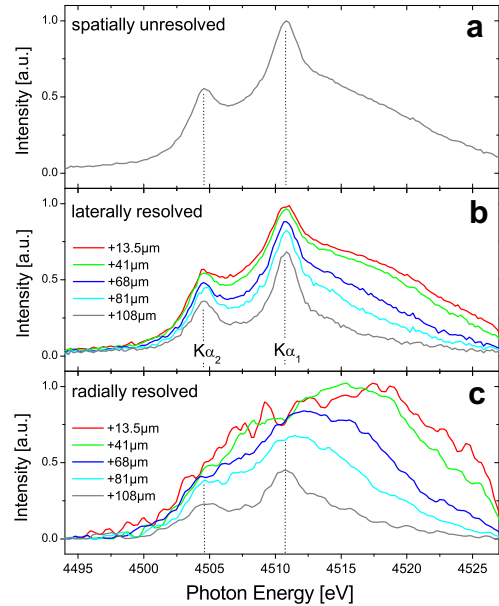


Fig. 6. Comparison of spectra obtained by (a) a spatially unresolved measurement, (b) the lateral one-dimensional resolution of the toroidally bent crystal spectrometer used in this paper, and (c) the radially resolved spectra obtain by Abel inversion.

independent of foil thickness. This is obviously not the case for the ω exposures. We consider several reasons for this observation: The differences are most likely related to the significantly suppressed laser–preplasma interaction due to the higher contrast ratio at 2ω . Hydrodynamics simulations for a typical ω exposure [43] show that as a result of the prepulse, the surface of the critical electron density $n_{\text{crit}} \approx 10^{21}$ cm^{-3} has moved ≈ 10 μm in front of the original metal foil surface. This results in a longer plasma scale length and more involved laser absorption mechanisms. Further, both intensity I and laser wavelength λ are reduced by about 50%, and the generated electrons will therefore be less energetic, since their effective temperature scales like $I\lambda^2$ [50,51]. As a likely consequence, their

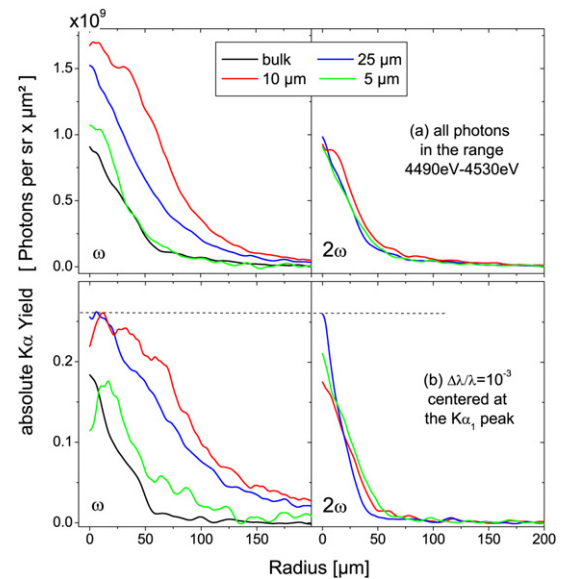


Fig. 7. Radially resolved $K\alpha$ yield ($\Delta x = 2.8$ μm) for irradiation using fundamental wavelength (left) and frequency doubled laser pulses (right). The energy on target was (13 ± 1) J and (8 ± 1) J, respectively. Both the yield in the full spectral range of the spectrometer (top), as well as a small spectral window centered at the $K\alpha_1$ -peak (bottom), are analyzed.

mean free path in the target foil is much shorter, filamentation and angular spread are reduced, and both E- and B-fields are less intense at 2ω irradiation.

A general increase of the plasma temperature for thinner foils was reported [31]. Therefore, we also irradiated a 2 μm thin pure titanium foil with the fundamental laser frequency. However, we did not observe a further increase in temperature compared to the 5 μm -foil. The prepulse at ω generates an energy density of $\sim 1 \text{ kJ}/\text{cm}^2$ at the focal spot within half a nanosecond. Hydrodynamics simulations using the one-dimensional HELIOS code [44] have been performed for the actual laser conditions. Fig. 8 shows the initial density profile and the results at timesteps of 0.1 ns. The first μm of the foil volume is ablated and expands into the vacuum, while the density in the remaining foil volume increases temporarily by $\leq 1.5 \times n_0$ due to a shock wave. When the main pulse arrives, after 0.5 ns, the surface of the foil has an involved density gradient.

In order to analyze the influence of the density gradient we calculate theoretical spectra as described above for a fixed temperature varying the target density according to the simulated density gradient. The foil profile 0.5 ns after irradiation was split into 10 slices. The average density of each slice was determined and the corresponding spectrum calculated. Assuming that the radiator density scales proportionally with the target density, the spectra were summed up weighted with the slice density and normalized to the intensity. Comparing the resulting spectrum with a spectrum calculated at the same temperature at standard solid target density, only minor changes of the line-shape were observed. The line profiles deviated about 4% for every considered temperature. Obviously, the shock-compressed area is too narrow and the preplasma density too small to significantly contribute to the spectral profile. Here we use typical temperatures at the plasma center for different foils, i.e. 24 eV, 33 eV, 40 eV, and 46 eV, respectively. From the simulations we further find that the density gradient affects mainly the first 2 μm of the foil depth and plays no role for thicker foils.

We may recall from the description of the experimental setup in Section 2 that the thinnest considered foil with 5 μm thickness was covered by 250 nm of copper. Since the fraction of hot preplasma, compared to the warm dense bulk material, is increasing with thinner foils, we wanted to suppress $K\alpha$ emission from the preplasma. By confining the preplasma mainly to the copper layer, it does not contribute to the titanium $K\alpha$ x-rays we measure from the frontside. Note that the copper layer may lead to a slightly decreased titanium $K\alpha$ yield in the regions far from the laser spot,

where the copper is not ablated during the emission in the first picoseconds.

5. X-ray yield and electron distribution

The conversion efficiency of optical laser energy into x-ray photons within a narrow bandwidth ΔE is a characteristic value relevant for time-resolved x-ray diffraction, backlighting applications such as shadowgraphy, or x-ray Thomson scattering [45]. For laser-driven x-ray sources with fs-pulse length, the absolute number of $K\alpha$ photons per laser energy ($1/\text{J}$) emitted in a 4π -sphere, or alternatively the conversion efficiency of laser energy to energy of $K\alpha$ photons is determined to compare with other experiments.

For the global $K\alpha$ yield, all photons from a single exposure are integrated over the spectral range. Fig. 9 shows seven individually measured yields: the data for three different foil thicknesses as well as bulk were analyzed for ω and 2ω laser frequency irradiation. For the ω exposures, we find a nearly constant yield for the 10 and 25 μm -foils. The yield decreases by a factor of 2.5 for bulk and the 5 μm -foil. This complex dependence on the foil thickness is remarkable, because a more systematic behavior would have been expected. The exposures at 2ω show a similar but less pronounced dependence on foil thickness.

In order to predict the tendency of the measured x-ray yield, we first assume that a fraction of the laser energy is converted into a relativistic electron distribution. Its temperature T_{hot} is determined by the laser intensity and wavelength. Secondly, we employ Monte-Carlo (MC) simulations [5] to calculate the conversion efficiency η_{ex} from electrons into K-shell vacancies, which in turn recombine by emitting $K\alpha$ photons.

So far, our results contain three-dimensional information on the characteristic x-ray emission of the generated plasma, but we have no measured information on the distribution of electrons, neither in space nor energy. Nevertheless, we can draw conclusions from the x-ray emission by applying the relativistic cross-section σ_K for titanium K-shell ionization [46] due to collisions with fast electrons. This cross-section reaches a maximum at electron energies of 15 keV, and has an approximately 60% lower but nearly constant value for $E > 100 \text{ keV}$. In this model, no effects from strong E- and B-fields are accounted for, nor are filamentation and other three-dimensional effects taken into account. Therefore, we restrict ourselves to a one-dimensional MC calculation to predict the integrated global $K\alpha$ yield.

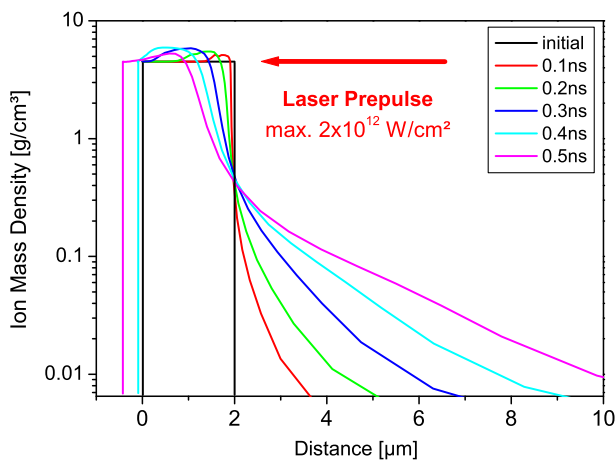


Fig. 8. Hydrodynamics simulation of the laser prepulse hitting a 2 μm Ti foil using the 1D HELIOS code. The prepulse is assumed as a linear ramp, reaching $2.5 \times 10^{12} \text{ W}/\text{cm}^2$ after 0.5 ns. At this time, the main pulse arrives and interacts with both a lower-density preplasma and $\sim 1.5 \times$ compressed residual foil.

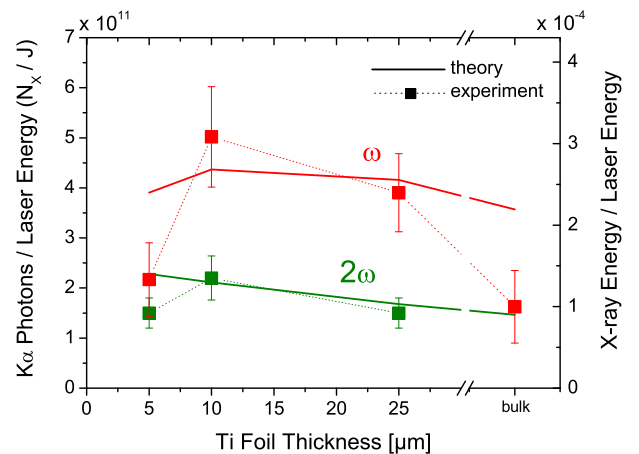


Fig. 9. The $K\alpha$ yield ($E = 4490\text{--}4530 \text{ eV}$) per incident laser energy as a function of target thickness. The right ordinate shows the ratio of x-ray energy to laser energy. The squares represent our measurements, while the solid lines are theoretical values deduced from Fig. 10. To match our experimental results, a conversion of laser energy into electrons of 50% was assumed for ω , and 10% for 2ω , respectively.

A fraction of fast electrons with kinetic energies $E \geq 500$ keV escapes the target and can be detected [11]. This charge-separation is the source of strong electric fields up to MV/ μm [47] at the foil boundaries. In contrast, the mean free path of fast electrons with $E < 100$ keV is of the order of tens of micrometers, but they are most probably confined to the target foil by the strong electric field and deposit their kinetic energy inside the foil by traversing it several times ('refluxing'). Thus, electrons with energies up to a few hundred keV are the dominant source of K-hole creation.

The properties of K-shell emission as discussed within this paper are sensitive to the low-energy part of the electron distribution: while electrons with $E \geq 5$ keV are capable of K-shell ionization, excitation and ionization of weakly bound electrons is dominated by slower electrons. These affect the $K\alpha$ line-shape by blue shifting, as observed in the presented data, and serve as bulk electron temperature indicator. This picture is further complicated by effects like secondary electrons, radiation heating and electron–electron interaction.

As initial electron distribution, a relativistically-correct Maxwell–Jüttner function is assumed. If these electrons traverse the foil only once, i.e. refluxing is neglected, thicker foils will emit more photons, only limited by reabsorption, as shown in the dashed curve in Fig. 10. This is in clear contrast to our observations (Fig. 9). Other models [48] account for total refluxing, i.e. all electrons are confined to the target foil. These models predict a constant yield independent of foil thickness. So, they cannot reproduce our observed dependence on foil thickness.

Thus, we extended the MC model to account for partial refluxing: electrons with an energy $E > E_{crit}$ are assumed to escape the target space-charge, while slower electrons are reflected inside the foil boundaries. The solid curves in Fig. 10 show that if $E_{crit} = 100$ keV is assumed, the overall efficiency is increased. For the 5–10 μm foils, it reaches a maximum of $\eta_{ex} = 1.3\%$ at $T_{hot} = 50$ keV, while it is only around 0.4% at $T_{hot} \geq 1$ MeV. For thicker foils, the effect of refluxing electrons is less pronounced, and it is negligible for bulk material. Qualitative agreement with our measurements (Fig. 9) regarding the target thickness dependence at ω is achieved at electron temperatures around 100 keV. Let us therefore assume an electron distribution with $T_{hot} = 100$ keV for all exposures at ω laser frequency.

For the high-contrast exposures at 2ω , it was shown [18] that the number of hot electrons injected into the solid is smaller for two reasons: (1) pre-ionization is suppressed and therefore the laser

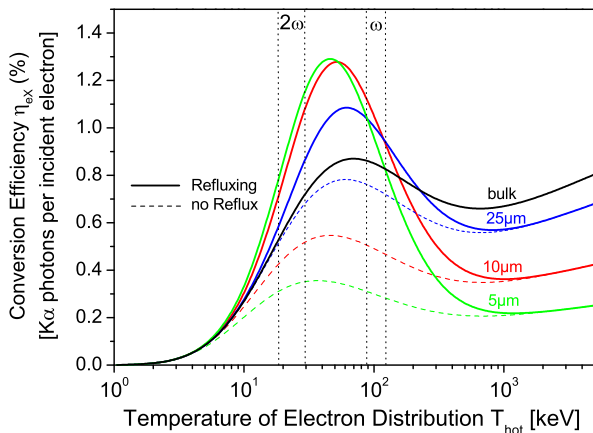


Fig. 10. The theoretical conversion efficiency of an electron distribution with T_{hot} into $K\alpha$ photons for different Ti foil thicknesses. The solid lines account for refluxing of electrons with $E < 100$ keV, compared to the dashed lines without refluxing. The marked areas indicate the electron temperature estimate for the ω and 2ω exposures, respectively.

pulse interacts with a steep density gradient [49], and (2) the temperature of the electron distribution scales with $T_{hot} \sim (I\lambda^2)^{0.3-0.5}$ [50,51]. Here, I is the laser intensity which is about 50% lower for the frequency doubled laser beam compared to the fundamental one, and λ is its wavelength. Thus, we get $T_{hot}^{2\omega} = (0.35 - 0.5)T_{hot}^{1\omega}$. These mechanisms are counterbalanced by the fact that more laser energy can be brought into the target, because the critical density is higher for shorter wavelengths, and preplasma formation is strongly suppressed [43].

From these scaling laws, the hot electron temperature for 2ω is then assumed to be of the order of 35 keV. An upper limit for the number of electrons is inferred by assuming that 100% of the incident laser energy is converted into electrons, independent of target thickness. Then we apply the conversion efficiency from Fig. 10 and gain a prediction for the $K\alpha$ yield. In order to match this result with the experimental data as shown in Fig. 9, we have to decrease the conversion of laser energy into hot electrons to 50% and 10% for ω and 2ω , respectively. Within typical error bars, these numbers agree well with previously published values [48,52,53].

At the fundamental wavelength, the large amount of free electrons in the preplasma result in an increased luminosity, compared to the exposures at 2ω , and are probably also the reason for the larger emission area shown in Fig. 5. The production of K-shell vacancies strongly depends on electrons at only several tens of keV within the first picosecond after irradiation. Thus, our electron temperatures are valid for the distribution of such keV electrons inside the target volume.

Note that in our experiments, at intensities of several 10^{19} W/cm², the peak of the hot electron distribution does not overlap with the peak of the K-shell ionization cross-section [5,54]. Therefore, the intensity is about two orders of magnitude too high for optimal $K\alpha$ production in titanium.

6. Brilliance limitations

Laser-driven x-ray sources are suitable to probe the dynamics of solid-density plasma [55]. Prominent examples are time-resolved x-ray diffraction or x-ray Thomson scattering. Maximum yield and short duration of the x-ray emission are crucial in both cases. Additionally, the latter case requires a narrow bandwidth of $\Delta E/E = 0.01$ for non-collective scattering [56] and $\Delta E/E = 0.002$ for collective scattering [57], respectively. Straightforwardly, from our findings, the plasma emits the narrow line-shape suitable for collective scattering only if its temperature does not significantly exceed 20 eV. Beyond this temperature, the spectral emission is broadened and blue-shifted, which would also limit the application

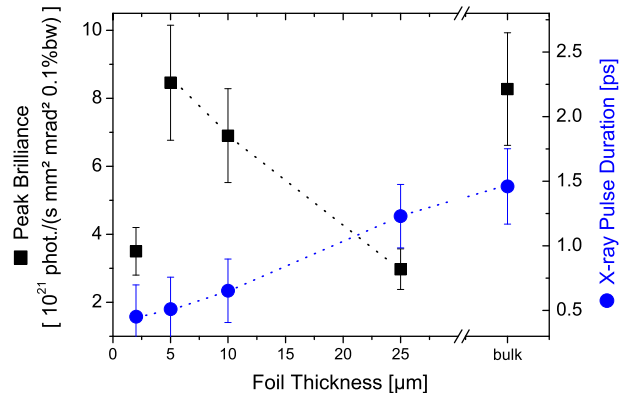


Fig. 11. Peak brilliance (squares) and estimated x-ray pulse duration (circles) as a function of foil thickness for irradiation at the laser fundamental frequency. A foil thickness of 5–10 μm fulfills both high brilliance and sub-picosecond pulse duration.

in x-ray optics such as monochromatic imaging [33]. As discussed regarding the radially resolved yield in Fig. 7, the concentration of cold $K\alpha$ emitters may be significantly reduced in case of highest irradiation intensities. The use of thicker foils on the other hand results in a longer x-ray pulse duration [5].

Gathering our results and applying the x-ray pulse duration inferred from our Monte-Carlo simulations, we plot the peak brilliance in Fig. 11 as a function of foil thickness. Note that the pulse duration is prolonged by 20 fs to 40 fs due to the refluxing electrons. As illustrated in Fig. 8, the laser ASE prepulse evaporates $\sim 50\%$ of the 2 μm -foil, which results in a decreased emitted photon number. A foil thickness of 5–10 μm fulfills both high brilliance and sub-picosecond pulse duration, while the bulk target emits a ~ 1.5 ps pulse.

7. Final conclusions and outlook

We employ high-resolution x-ray spectroscopy with toroidally bent crystals, and derive radially resolved, single-pulse, absolutely calibrated $K\alpha$ spectra emitted by thin Ti foils irradiated by relativistic laser intensities. The temperature of solid-density plasmas is inferred with a radial resolution of 13.5 μm in a single exposure.

We observe a heated central spot with a radius between 25 and 80 μm depending on laser parameters and target thickness. It is surrounded by a steep temperature gradient. The line-shape at the emission center changes drastically. Compared to the cold $K\alpha$ doublet at large radii, we observe a single broad line with an FWHM of 20 eV. Further the central photon energy is blue-shifted to 4514 eV. The radiation is emitted by solid-density plasma with temperatures up to 50 eV.

We also measured the $K\alpha$ yield as a function of target thickness d and observe a maximum yield for foil thicknesses of 10–25 μm . These results are explained by means of the electron refluxing model. Hence we derive parameters to optimize the brilliance of such x-ray sources. This study extends the development of plasma diagnostics for shock wave physics, applied material studies, planetary physics, inertial confinement fusion, and other forms of high energy density matter generation.

Further research in this field will concentrate on the plasma temperature, studies as function of target thicknesses, time-resolved measurements of the x-ray emission by means of streak-cameras, and the contribution of refluxing electrons.

Acknowledgments

We thankfully acknowledge financial support by the German Research Foundation (DFG), the German–Israeli Foundation for Scientific Research and Development (GIF) via grant No I-880-135.7/2005, and the German Federal Ministry for Education and Research (BMBF) via project FSP 301-FLASH.

References

- [1] R.W. Lee, et al., *Laser Part. Beams* 20 (2002) 527.
- [2] J. Lindl, et al., *Phys. Plasmas* 11 (2004) 339–491.
- [3] M. Tabak, J. Hammer, et al., *Phys. Plasmas* 1 (1994) 1626–1634.
- [4] T.R. Dittrich, et al., *Phys. Plasmas* 6 (1999) 2164.
- [5] C. Reich, et al., *Phys. Rev. Lett.* 84 (2000) 4846–4849.
- [6] H.-S. Park, N. Izumi, et al., *Rev. Sci. Instrum.* 75 (2004) 4048–4050.
- [7] O.L. Landen, D.R. Farley, et al., *Rev. Sci. Instrum.* 72 (2001) 627–634.
- [8] A. Pukhov, J.M. ter Vehn, *Phys. Rev. Lett.* 76 (1996) 3975–3978.
- [9] W. Leemans, et al., *Nat. Phys.* 2 (2006) 696–699.
- [10] H. Schwoerer, et al., *Nature* 439 (2006) 445–448.
- [11] G. Malka, M. Aeonard, et al., *Phys. Rev. E* 66 (2002) 066402.
- [12] G. Malka, P. Nicolai, et al., *Phys. Rev. E* 77 (2008) 026408.
- [13] A. Saemann, et al., *Phys. Rev. Lett.* 82 (1999) 4843–4846.
- [14] P. Gibbon, et al., *Plasma Phys. Contr. Fusion* 38 (1996) 769–793.
- [15] J. Gordon, *Phys. Rev. A* 8 (1973) 14–21.
- [16] T. Feurer, W. Theobald, et al., *Phys. Rev. E* 56 (1997) 4608–4614.
- [17] B. Hidding, et al., *Rev. Sci. Instrum.* 78 (2007) 083301.
- [18] R. Evans, HEDP, vol. 1 (2006) pp. 35–47.
- [19] A. Robinson, M. Sherlock, *Phys. Plasmas* 14 (2007) 083105.
- [20] L.B. Da Silva, et al., *Phys. Rev. Lett.* 78 (1997) 483.
- [21] J. MacFarlane, et al., *Phys. Rev. E* 47 (1993) 2748–2758.
- [22] J. Bailey, et al., *Phys. Rev. E* 56 (1997) 7147–7158.
- [23] T. Kawamura, et al., *Laser Part. Beams* 24 (2006) 261.
- [24] T. Ao, et al., *Phys. Rev. Lett.* 96 (2006) 055001.
- [25] T. Kawamura, et al., *J. Quant. Spectrosc. Radiat. Transf.* 81 (2003) 237246.
- [26] H. Nishimura, T. Kawamura, et al., *J. Quant. Spectrosc. Radiat. Transf.* 81 (2003) 327–337.
- [27] U. Zastrau, C. Fortmann, et al., *Phys. Rev. E* 78 (2008) 066406.
- [28] B. Nagler, U. Zastrau, et al., *Nat. Phys.* 5 (2009) 693–696.
- [29] S. Chen, et al., *Phys. Plasmas* 14 (2007) 102701.
- [30] U. Zastrau, P. Audebert, et al., *Phys. Rev. E* 78 (2010) 066406.
- [31] S. Hansen, et al., *Phys. Rev. E* 72 (2005) 036408.
- [32] B. Wattellier, et al., *J. Opt. Soc. Am. B* 20 (2003) 1632–1642.
- [33] T. Missalla, et al., *Rev. Sci. Instrum.* 70 (1999) 1288–1299.
- [34] H. Johann, *Zeitschrift für Physik* 69 (1931) 185–206.
- [35] F. Zamponi, et al., HEDP, vol. 3 (2007) pp. 297–301.
- [36] M. Zepf, E. Clark, et al., *Phys. Plasmas* 8 (2001) 2323–2330.
- [37] H. Nguyen, et al., *Phys. Rev. A* 33 (1986) 1279.
- [38] A. Sengebusch, et al., *J. Phys. A Math. Gen.* 42 (2009) 214061.
- [39] A. Sengebusch, H. Reinholz, G. Röpke, *Contrib. Plasma Phys.* 49 (2009) 748.
- [40] D. Kremp, M. Schlages, W.D. Kraeft, *Quantum Statistics of Nonideal Plasmas*. Springer Berlin, 2005.
- [41] E. Stambulchik, et al., *J. Phys. A Math. Gen.* 42 (2009) 214056.
- [42] D. Anagnostopoulos, D. Gotta, P. Indelicato, L. Simons, *Phys. Rev. Lett.* 91 (2003) 240801.
- [43] S.D. Baton, M. Koenig, et al., *Phys. Plasmas* 15 (2008) 042706.
- [44] J. MacFarlane, et al., *J. Quant. Spectrosc. Radiat. Transf.* 99 (2006) 381.
- [45] S.H. Glenzer, et al., *Phys. Rev. Lett.* 98 (2007) 065002.
- [46] E. Casnati, A. Tartari, C. Baraldi, *J. Phys. B Atom. Mol. Phys.* 15 (1982) 155–167.
- [47] R. Snavely, M. Key, et al., *Phys. Rev. Lett.* 85 (2000) 2945–2948.
- [48] W. Theobald, K. Akli, et al., *Phys. Plasmas* 13 (2006) 043102.
- [49] S. Bastiani, A. Rousse, et al., *Phys. Rev. E* 56 (1997) 7179–7185.
- [50] S. Wilks, W. Krueer, et al., *Phys. Rev. Lett.* 69 (1992) 1383–1386.
- [51] F. Beg, A. Bell, et al., *Phys. Plasmas* 4 (1997) 447–457.
- [52] F. Khattak, A.-M. McEvoy, et al., *J. Phys. D* 36 (2003) 2372–2376.
- [53] F. Ewald, H. Schwoerer, R. Sauerbrey, *Europhys. Lett.* 60 (2002) 710–716.
- [54] C. Reich, et al., *Phys. Rev. E* 68 (2003) 056408.
- [55] A. Rousse, et al., *Nature* 410 (2001) 65–68.
- [56] O.L. Landen, et al., *J. Quant. Spectrosc. Radiat. Transf.* 71 (2001) 465.
- [57] M. Urry, G. Gregori, et al., *J. Quant. Spectrosc. Radiat. Transfer* 99 (2006) 636–648.